TRPA1 modulation by piperidine carboxamides suggests an evolutionarily conserved binding site and gating mechanism

Tania Chernov-Rogan[a,1], Eleonora Gianti[b,1,2], Chang Liu[a], Elisia Villemure[c], Andrew P. Cridland[d], Xiaoyu Hu[a,3], Elisa Ballini[e], Wienke Lange[e], Heike Deisemann[e], Tianbo Li[a], Stuart I. Ward[d], David H. Hackos[f], Steven Magnuson[c], Brian Safina[c,4], Michael L. Klein[b], Matthew Volgraf[c], Vincenzo Carnevale[b,2], and Jun Chen[a,2]

[a]Biochemical and Cellular Pharmacology, Genentech, Inc., South San Francisco, CA 94080; [b]Institute for Computational Molecular Science, Department of Chemistry, Temple University, Philadelphia, PA 19122; [c]Discovery Chemistry, Genentech, Inc., South San Francisco, CA 94080; [d]Charles River, CM19 5TR Harlow, Essex, United Kingdom; [e]Ion Channel Group, Evotec AG, 22419 Hamburg, Germany; and [f]Neuroscience, Genentech, Inc., South San Francisco, CA 94080

Edited by Richard W. Aldrich, The University of Texas at Austin, Austin, TX, and approved November 5, 2019 (received for review August 15, 2019)

The transient receptor potential ankyrin 1 (TRPA1) channel functions as an irritant sensor and is a therapeutic target for treating pain, itch, and respiratory diseases. As a ligand-gated channel, TRPA1 can be activated by electrophilic compounds such as allyl isothiocyanate (AITC) through covalent modification or activated by noncovalent agonists through ligand binding. However, how covalent modification leads to channel opening and, importantly, how noncovalent binding activates TRPA1 are not well-understood. Here we report a class of piperidine carboxamides (PIPCs) as potent, noncovalent agonists of human TRPA1. Based on their species-specific effects on human and rat channels, we identified residues critical for channel activation; we then generated binding modes for TRPA1–PIPC interactions using structural modeling, molecular docking, and mutational analysis. We show that PIPCs bind to a hydrophobic site located at the interface of the pore helix 1 (PH1) and S5 and S6 transmembrane segments. Interestingly, this binding site overlaps with that of known allosteric modulators, such as A-967079 and propofol. Similar binding sites, involving π-helix rearrangements on S6, have been recently reported for other TRP channels, suggesting an evolutionarily conserved mechanism. Finally, we show that for PIPC analogs, predictions from computational modeling are consistent with experimental structure–activity studies, thereby suggesting strategies for rational drug design.

TRPA1 | agonist | binding | gating

The transient receptor potential ankyrin 1 (TRPA1) channel is a nonselective cation channel belonging to the TRP superfamily (1, 2). In the somatosensory system, TRPA1 is highly expressed in small- and medium-sized sensory neurons; TRPA1 gene knockout and antagonist treatment attenuate pain in several rodent models (3–6); and, in humans, a gain-of-function mutation of TRPA1 is linked to familial episodic pain syndrome (7). TRPA1 is also implicated in histamine-independent itch (8), and genetic ablation or pharmacological blockade of TRPA1 decreases oxidative stress-evoked scratching (9). In the respiratory system, TRPA1 is expressed in primary sensory neurons innervating the airways, where it acts as a chemosensor for airway irritants (10). Together, these studies have established TRPA1 as a promising therapeutic target (11).

A functional TRPA1 channel is composed of 4 identical subunits, each containing 6 transmembrane (TM) segments (S1 to S6), intracellular N and C termini, and an ion conduction pore formed between the S5 and S6 segments. As a ligand-gated channel, TRPA1 can be activated by a variety of stimuli, including intracellular Ca^{2+}, hypertonicity, amphipathic molecules (12–14), and, most notably, by a plethora of electrophilic compounds, including pungent natural products (e.g., allyl isothiocyanate; AITC), environmental irritants (e.g., acrolein), and reactive metabolites (e.g., 4-hydroxynonenal) (1, 15–17). These electrophilic compounds activate TRPA1 by covalently modifying cysteine residues in the N terminus of the channel protein (15, 16). A number of TRPA1 antagonists have also been discovered, including A-967079 (4). The binding site of A-967079, located in the pore domain, was first determined through a mutagenesis approach (18, 19) and then confirmed by the presence of a density map, compatible with a ligand, in the cryoelectron microscopy (cryo-EM) structure (20). Besides TRPA1, cryo-EM structures have recently been determined for many other TRP channels, including TRPML1, TRPML3, TRPV1, TRPV5, TRPV6, and TRPM8, thereby revealing unprecedented insights into the mechanisms of channel gating and regulation (21–27). Despite these recent discoveries, how TRPA1 responds to covalent modification and noncovalent agonist binding is not well-understood.

Significance

The TRPA1 channel functions as an irritant sensor and is a therapeutic target for treating pain, itch, and respiratory diseases. TRPA1 can be activated by electrophilic compounds via covalent modification or activated by noncovalent agonists via ligand binding. However, how covalent modification leads to channel opening and, importantly, how noncovalent binding activates TRPA1 are not well-understood. Here we identified a group of noncovalent agonists and used them to explore TRPA1 gating through iterative functional analyses, molecular modeling, and structure–activity relationship studies. We show that TRPA1 possesses an evolutionarily conserved ligand binding site common to other TRP channels. The combination of computational modeling and experimental structure–activity data lays the foundations for rational drug design.

Author contributions: V.C. and J.C. designed research; T.C.-R., E.G., C.L., E.V., A.P.C., E.B., W.L., and H.D. performed research; E.V., A.P.C., X.H., T.L., S.I.W., D.H.H., S.M., B.S., M.L.K., M.V., and J.C. contributed new reagents/analytic tools; T.C.-R., E.G., C.L., and J.C. analyzed data; and E.G., V.C., and J.C. wrote the paper.

The authors declare no competing interest.

This article is a PNAS Direct Submission.

[1]T.C.-R. and E.G. contributed equally to this work.

[2]To whom correspondence may be addressed. Email: egianti@temple.edu, vincenzo.carnevale@temple.edu, or chenj144@gene.com.

[3]Present address: Department of Stem Cell and Regenerative Biology, Harvard University, Cambridge, MA 02138.

[4]Present address: Bolt Biotherapeutics, Inc., Redwood City, CA 94063.

This article contains supporting information online at https://www.pnas.org/lookup/suppl/doi:10.1073/pnas.1913929116/-/DCSupplemental.

First published December 3, 2019.

In the current study, we identified a group of noncovalent agonists and used them to explore the gating mechanism of TRPA1. Through iterative functional analyses, molecular modeling, and structure–activity relationship (SAR) studies, we show an evolutionarily conserved ligand binding site and gating mechanism. By combining computational modeling with experimental structure–activity studies, we lay the foundations for rational drug design.

Results

Piperidine Carboxamides as Potent Agonists of Human TRPA1. We characterized a family of TRPA1 modulators bearing the piperidine-carboxamide (PIPC) moiety, including PIPC1 and PIPC2 (Fig. 1). Although PIPC2 was previously characterized as an antagonist (denoted as compound 39) due to its inhibition of cinnamaldehyde-evoked human TRPA1 currents (28), we found that the primary effect of PIPCs is the activation of human TRPA1. In HEK-293F cells transiently expressing human TRPA1, PIPC1 (10 nM) and PIPC2 (40 nM) induced robust Ca^{2+} influx, whereas A-967079, a known TRPA1 antagonist (4), did not induce Ca^{2+} influx (Fig. 1*A*). At higher concentrations, PIPC1 (100 nM) and PIPC2 (400 nM) also evoked rapid Ca^{2+} influx, but the signals decayed over time; also, the applications of PIPC1 and PIPC2 prevented the response to AITC, suggesting channel desensitization. Furthermore, PIPC1- and PIPC2-evoked responses were blocked by preincubation with A-967079, indicating that PIPC1- and PIPC2-evoked responses are specific to the TRPA1 channel (Fig. 1*B*). Compared with AITC, PIPC1 and PIPC2 are much more potent (EC_{50} = 0.0065 ± 0.0011 μM for PIPC1; 0.026 ± 0.003 μM for PIPC2; 13 ± 0.7 μM for AITC; n = 4) but are less efficacious (E_{max} = 46 ± 1.3% for PIPC1; 26 ± 0.9% for PIPC2; n = 4; Fig. 1*C*).

The effects of PIPC1 and PIPC2 were further confirmed using whole-cell patch-clamp electrophysiology. CHO cells stably expressing human TRPA1 were perfused with a nominally Ca^{2+}-free external solution to reduce channel desensitization (29). From a holding voltage at −60 mV, a 200-ms voltage ramp (from −80 to +80 mV) was applied repetitively once every second. PIPC1 (10 nM) and PIPC2 (30 nM) evoked currents, which could be blocked by coapplication of 10 μM A-967079 (Fig. 1*D*). At higher concentrations, PIPC1 (300 nM) and PIPC2 (1.2 μM) activated and desensitized the channel, and prevented further response to AITC (100 μM). To quantitate the effect of PIPC1 and PIPC2,

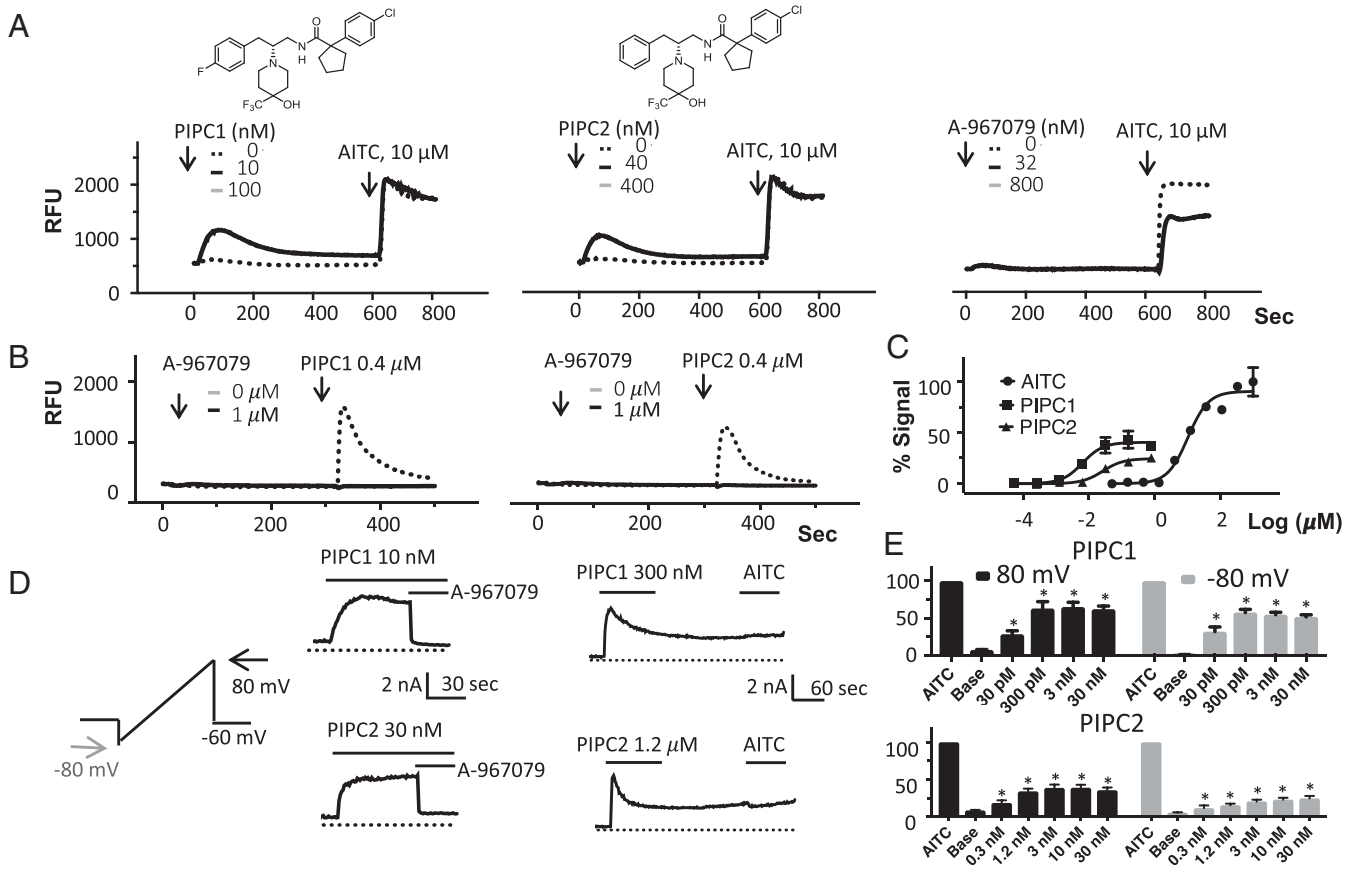

Fig. 1. Piperidines activate human TRPA1. (*A*) Structure and activity of PIPC1 and PIPC2. PIPC1 and PIPC2 evoked Ca^{2+} influx in HEK-293F cells expressing human TRPA1, as represented by an increase in fluorescence signal (RFU, relative fluorescence unit). In contrast, A-967079 did not evoke Ca^{2+} response and blocked AITC-evoked responses. Of note, the responses to 100 nM PIPC1 or 400 nM PIPC2 decayed over time and prevented subsequent response to 100 μM AITC. n = 4 to 8. (*B*) PIPC1- (0.4 μM) and PIPC2- (1 μM) induced Ca^{2+} influx was blocked by preincubation of A-967079 (1 μM). n = 4 to 8. (*C*) Concentration dose–response of PIPC1 and PIPC2. PIPC1- and PIPC2-induced Ca^{2+} signals were normalized against the effect of 300 μM AITC. n = 4. Hill slopes were 1.5, 1.4, and 1.4 for PIPC1, PIPC2, and AITC, respectively. (*D*) In representative cells expressing human TRPA1, PIPC1 (10 nM) or PIPC2 (30 nM) evoked currents that were sensitive to block by A-967079 (10 μM). At high concentrations, PIPC1 (300 nM) and PIPC2 (1.2 μM) evoked fast-onset currents, followed by current decay and insensitivity to AITC (100 μM). Dark trace: current at +80 mV; gray trace: current at −80 mV; dotted line: 0-current level. n = 4 to 8. (*E*) Relative current amplitudes at baseline (Base) and in response to varying concentrations of PIPC1 or PIPC2. Each cell was stimulated with a single concentration of compounds, and currents were normalized against peak currents of 100 μM AITC obtained from a different group of cells. The asterisk indicates significantly different (*P < 0.001) from baseline. n = 13 to 25. Representative traces are shown. The apparent potency of PIPC1 and PIPC2 from patch-clamp experiments could be overestimated, due to desensitization and the use of divalent-free solution. However, qualitatively, these patch-clamp experiments confirmed the agonist effect of PIPC1 and PIPC2.

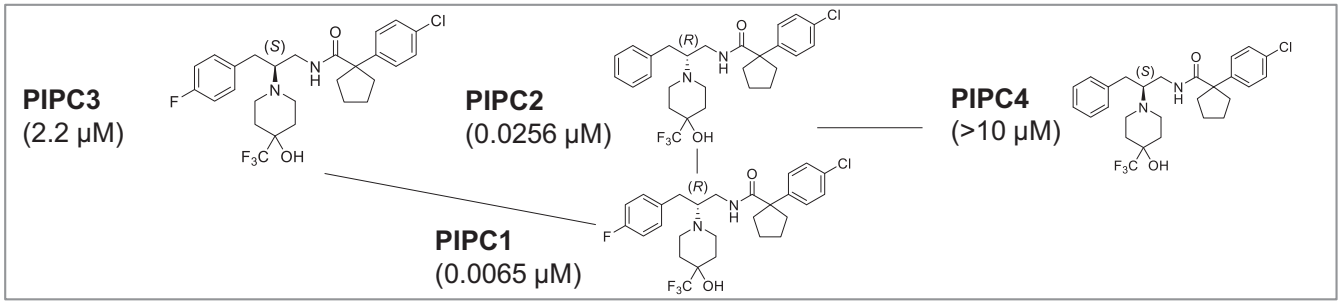

Scheme 1. Structure–activity relationship for PIPC1 to PIPC4.

we compared current amplitudes before and after a single treatment with varying concentrations of PIPC1 and PIPC2 (Fig. 1*E*). Together, these studies indicate that PIPC1 and PIPC2 are potent but partial agonists of human TRPA1.

Among the piperidine-carboxamide series, PIPC1 (Scheme 1) is the most potent TRPA1 agonist (EC_{50} = 6.5 nM), followed by PIPC2, a close analog lacking a fluorine on the aryl left-hand side (EC_{50} = 26 nM). Interestingly, we found that the potency was drastically affected by the chirality at the piperidine center: The EC_{50} for (*S*)-enantiomers of PIPC1 (i.e., PIPC3) was 2.2 μM, and the EC_{50} for the (*S*)-enantiomer of PIPC2 (i.e., PIPC4) was >10 μM. The severe loss in potency of (*S*)-enantiomers suggested that the substituted piperidine ring may play a crucial role in interacting with the channel.

Residues Critical for TRPA1 Activation by PIPC1 and PIPC2. We and others previously showed that many TRPA1 ligands have species-specific effects (18, 29–31). Therefore, we tested PIPC1 against TRPA1 from several species, including human, rat, dog, guinea pig, and chicken. In the Ca^{2+} assays, all channels produced robust response to AITC (Fig. 2*A*). In contrast, PIPC1 activated human TRPA1 but not rat, dog, guinea pig, or chicken TRPA1, indicating a species-specific effect (Fig. 2*A*).

To identify the molecular basis of PIPC1 activation of human TRPA1, we constructed rat–human TRPA1 (rTRPA1–hTRPA1) chimeras by systematically transferring various domains of the rat channel into the human channel background (Fig. 2*B*). Chimeric channels containing rat N terminus (rN), PreS1 domain (rPreS1), voltage sensor domain (rVSD), or C terminus (rC) retained human channel-like sensitivity to PIPC1. By contrast, introducing rat S5/S5–S6 linker (rS5P) or S6 segment (rS6) greatly reduced activity of PIPC1. These findings suggested that the S5/S5–S6 linker and S6 segment may underlie the species-specific effect.

The sequence alignment for the S5–S6 linker and S6 segment of human and rat TRPA1 revealed 16 nonconserved residues (Fig. 3*A*). Each of the 16 residues in human TRPA1 was substituted with the equivalent rat TRPA1 residue either individually (e.g., V875G) or in combination (e.g., E920D/S921A). Most mutations (e.g., I890V) retained activation by PIPC1; in contrast, 2 single-residue substitutions, I946M in the S6 segment and V875G in the S5 segment, abolished activation by PIPC1 (Fig. 3 *A*–*C*). Remarkably, a double mutation (rG878V/M849I) restored sensitivity to PIPC1 (Fig. 3 *B* and *C*). In patch-clamp experiments, PIPC1 evoked currents in hTRPA1 and rG878V/M949I at 3 and 10 nM, respectively (Fig. 3*D*), whereas 300 nM PIPC1 failed to evoke currents in the I946M mutant. Similar results were obtained for PIPC2 in the Ca^{2+} assay (Fig. 3 *E* and *F*) and patch-clamp recordings (Fig. 3*G*). Therefore, V875 and I946 are necessary and sufficient for determining the species-specific activation by both PIPC1 and PIPC2.

A Binding Site Formed by the Pore Helix and Segments S5 and S6. To characterize interactions between TRPA1 and PIPCs, we generated 2 independent sets of structural models of the human TRPA1

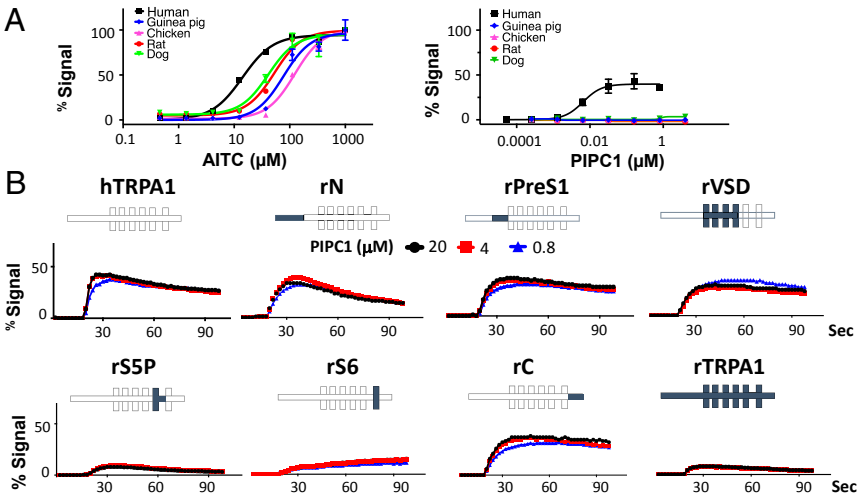

Fig. 2. Pore domain underlies the species-specific effect of PIPC1. (*A*) AITC activated TRPA1 from human, guinea pig, chicken, rat, and dog in a concentration-dependent manner, whereas PIPC1 only activated the human TRPA1 channel. Hill slope values for AITC were 1.4 to 1.7 for all species, and the Hill slope for PIPC1 was 1.6. (*B*) PIPC1 (20, 4, and 0.8 μM) evoked robust Ca^{2+} responses on hTRPA1, rN, rPreS1, rVSD, and rC but not on rS5P, rS6, or rTRPA1. Traces were normalized to the response evoked by 300 μM AITC. n = 4 to 8 for all experiments, and representative traces are shown.

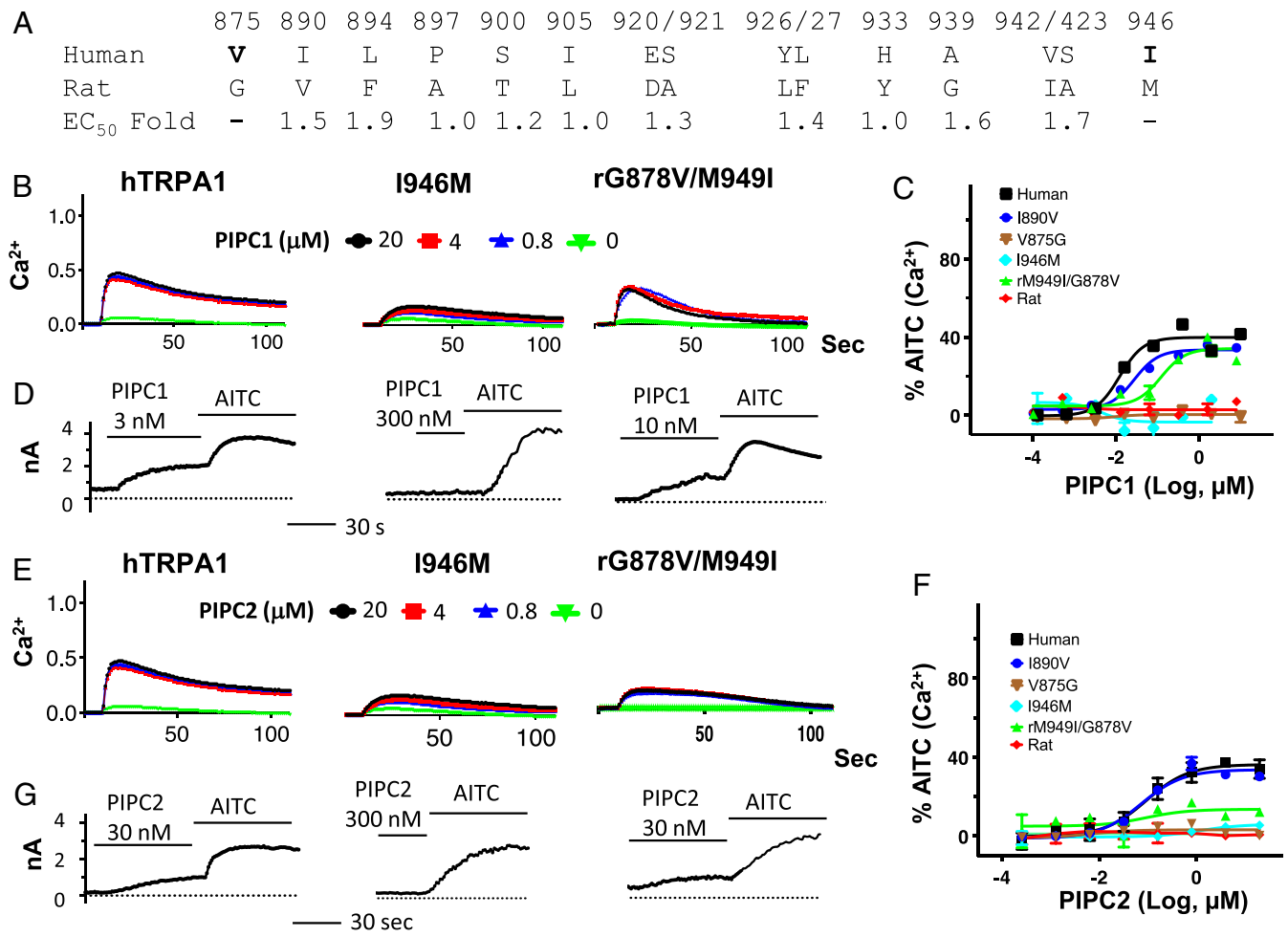

Fig. 3. V875 and I946 are critical for PIPC1 and PIPC2 activation of human TRPA1. (*A*) Divergent residues between human and rat channel in the S5, S5–S6 linker, and S6 segments. Each of the human TRPA1 residues was substituted by the equivalent residue in rat TRPA1 either individually or in combination; the fold change in PIPC1 potency is indicated below the sequences. V875G and I946M abolished response to PIPC1 whereas other mutations retained PIPC1 responses. (*B*) Representative Ca^{2+} influx traces in response to 20, 4, 0.8, and 0 μM PIPC1. I946M eliminated response to PIPC1, whereas rG878V/I949M restored response. $n = 4$ to 8. (*C*) Concentration–response relationships of PIPC1. EC_{50} and Hill slope values were 0.0065 ± 0.0003 μM and 1.5 for human TRPA1, 0.031 ± 0.04 μM and 1.4 for I890V, and 0.123 ± 0.006 μM and 1.5 for rG878V/M949I; E_{max} values (relative to AITC) were 0.41 ± 0.03 for human, 0.39 ± 0.04 for I890V, and 0.38 ± 0.06 for rG878V/M949I. $n = 4$. (*D*) Representative currents in response to PIPC1 and 100 μM AITC stimulation. The voltage protocol was the same as in Fig. 1*D* and currents at +80 mV are plotted. The dotted line indicates 0-current level. PIPC1 evoked currents in hTRPA1 and rG878V/M949I at 3 and 10 nM, respectively, but failed to induce current in I946M at 300 nM. $n = 6$ to 8. (*E*) Representative Ca^{2+} influx traces in response to PIPC2. $n = 4$ to 8. (*F*) Concentration–response relationships for PIPC2. EC_{50} and Hill slope values of PIPC2 were 0.026 ± 0.003 μM and 1.4 for hTRPA1, and 0.035 ± 0.06 μM and 1.4 for I890V. For rG878V/M949I, EC_{50} was not determined due to relatively small E_{max} (~0.16). $n = 4$. (*G*) Representative currents in response to PIPC2 and 100 μM AITC stimulation. PIPC2 (30 nM) activated currents in human TRPA1 and rG878V/M949I but had no effect on I949M. Representative traces are shown for all experiments.

channel in the closed and open states. First, we refined the experimental structure of TRPA1 in the closed state (20), using a previously described procedure (32) (Fig. 4*A* and *SI Appendix*, Fig. S1 *A–C*). Due to the lack of an experimental structure of open TRPA1, we used TRPV1 and TRPV6 as templates to generate additional models of TRPA1 in the open and closed states (26) (TRPV1-open state and TRPV6-open and -closed states) (Fig. 4 *B–E* and *SI Appendix*, Fig. S1 *D* and *E*). Analyses of models obtained using different templates highlighted optimal structural agreement between the TM domains of TRPA1 in different states (Fig. 4 *B–E* and *SI Appendix*, Fig. S1 *E–G*). Superimposition of the 2 open models of TRPA1 (modeled on TRPV1 and TRPV6) yielded near-identical conformations of S5, S6, and pore helix 1 (PH1) (Fig. 4*C*). Similarly, the 2 closed structures of TRPA1 (the refined TRPA1 structure and the model built on TRPV6) showed almost identical backbone superimposition (*SI Appendix*, Fig. S1*E*). Overlaps between the open and closed structures of TRPA1 suggested that similar structural changes occur during the closed-to-open transition (*SI Appendix*, Fig. S1*D*: open model on TRPV1, refined TRPA1 structure closed state; Fig. 4*D*: open and closed model on TRPV6) and pointed out significant rotation of S6 in the lower portion of the TM pores, similar to what was observed experimentally with TRPV6 (*SI Appendix*, Fig. S1 *F* and *G*).

Comparisons of the TM domains of closed and open TRPA1 channels (Fig. 4*A*) showed a clear difference at both the upper (D915) and lower (I957 and V961) gates, which are dynamically involved in the closed-to-open transition (20). In particular, the Cα-to-Cα distance between diagonally opposed D915 residues changes from 8.8 to 10.5 Å. Similarly, residues I957 and V961 separate farther upon channel opening, with a Cα-to-Cα distance changing from 11.5 to 14.0 Å and from 10.6 to 13.5 Å, respectively. Another interesting difference concerns the rearrangement of a π-bulge located on the S6 segment (residues 946 to 950), just below PH1 and the selectivity filter (Fig. 4*B*). The π-bulge on the S6 segment appears to be conserved within the TRP family (23, 26,

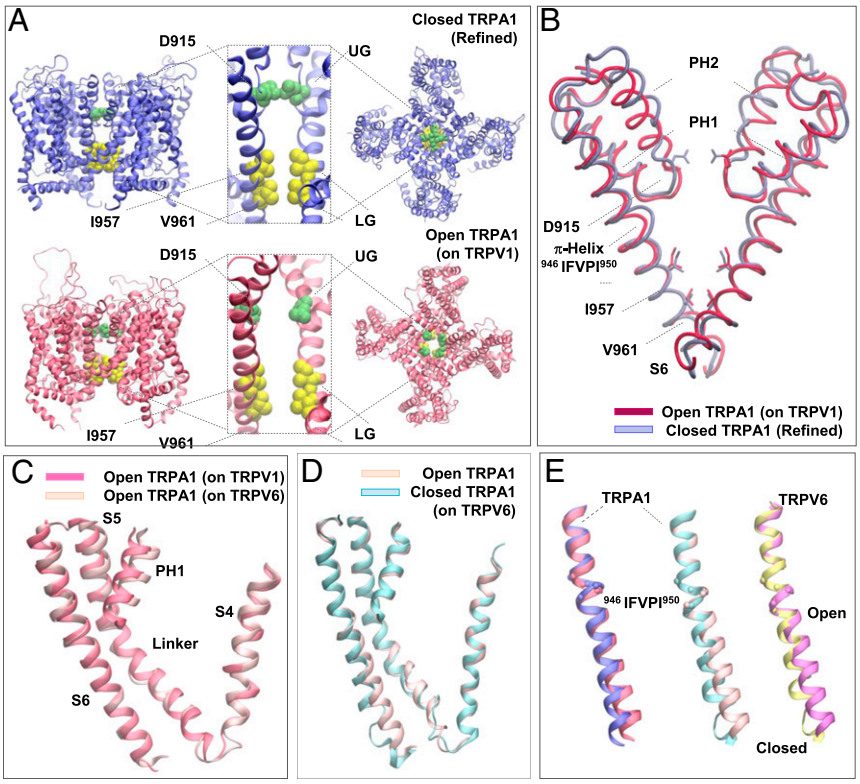

Fig. 4. Structural comparisons of closed and open TRPA1 states. (*A*) Homology models of TRPA1 in the closed (blue) and open states (red; TRPV1 as template). Only TM domains (residues 446 to 1078) are shown. TRPA1 structures are rendered as a cartoon. (*A*, *Left*) Side views. (*A*, *Middle*) Zoom into the pore structures. (*A*, *Right*) Top views. LG, lower gate; UG, upper gate. Only backbones are shown, with the exception of upper (D915) and lower gates (I957 and V961). (*B*) Closed and open TRPA1 states are superimposed along the pore helices (PH1 and PH2) and the S6 segments. For each state, PH1 and PH2, along with TM helical segment 6, are shown for 2 opposing subunits. S5 segments were removed from the visualization. Residues of S6 involved in the π-bulge rearrangement are labeled (^{946}IFVPI^{950}). (*C*) Superimposition of the 2 TRPA1 open models using TRPV1 and TRPV6 as templates (shown in red and pink, respectively). (*D*) Superimposition of TRPA1 structures in the open and closed states over residues in S5 and S6 helices and PH1. Models obtained using TRPV6 as template are shown in pink (open) and cyan (closed), respectively. (*E*) Superimposition of S6 segments from TRPA1 models and TRPV6 experimental structures (colored as in *A*–*D*).

33, 34) (Fig. 4*E* and *SI Appendix*, Fig. S1*G*), and will be discussed in detail.

To search for suitable sites for ligand binding and for structural changes associated with the closed-to-open transition, we used SiteMap, a computational approach, to exhaustively explore the surfaces of closed and open TRPA1 structures (35, 36) (also see *Materials and Methods* for details) and found several "spots" potentially suitable for ligand binding. These potential binding sites are mainly located on the intracellular side, far away from I946 and V875, the 2 residues identified experimentally as critical for TRPA1 activation by PIPC1 and PIPC2. Based on size, shape, hydrophobic properties, and druggability score >1, the topmost promising region is located in the TM domain of TRPA1 at the interface formed by S5 (hosting V875), PH1, and 2 S6 helices (hosting I946), the latter from adjacent subunits. Due to the 4-fold symmetry of TRPA1, 4 independent sites exist at equivalent locations in the tetrameric channel (Fig. 5*A* and *SI Appendix*, Fig. S2).

Interestingly, this binding spot, which is predicted to be highly druggable on the basis of size, shape, and hydrophobic character (*SI Appendix*, Fig. S2), lies near V875 and I946, 2 residues identified experimentally as critical for PIPC1 binding (Fig. 3). It is remarkable that this pocket coincides with the binding site of the antagonist A-967079 (20) (closed state; *SI Appendix*, Fig. S3) and with that of the agonists propofol and isoflurane (32, 37). Furthermore, F909, a PH1 residue critical for interactions with A-967079, propofol, and isoflurane, was also predicted to interact with PIPC1 (Fig. 5 *B* and *C*). Indeed, mutation of F909 to alanine (F909A) completely eliminated PIPC1 response (*SI Appendix*, Table S1). Of the additional binding spots evaluated, none were predicted to form "druggable" sites suitable for small-molecule binding. In addition, none of those sites featured residues shown experimentally to interact with PIPCs. Hence, based on experimental data and computational work, we surmise that the binding of PIPC1 to TRPA1 occurs at this location, and critical residues (V875, F909, and I946) either constitute an integral part of the binding site or are located in its proximity.

Piperidine Carboxamides Bind Primarily to the Open State. Next, we used molecular docking to generate binding hypotheses for PIPCs (see *Materials and Methods* for details) to the closed and open TRPA1 states, using both sets of structures (2 open and 2 closed states built on TRPV1 and TRPV6 and on TRPA1 and TRPV6, respectively). We observed that both volume and hydrophobic character of the putative site change significantly upon the closed-to-open transition; in particular, the pocket becomes much larger in the open state (*SI Appendix*, Fig. S2). Furthermore, due to the π-bulge rearrangement that occurs upon channel opening (Fig. 4*B*), the C-terminal end of S6 rotates significantly, resulting in exposing different sets of residues to the binding site in each of the 2 states (Fig. 4 *B*–*E*), a behavior previously observed in other TRP channels (26, 33, 34).

According to our data, binding of PIPCs to TRPA1 occurs primarily in the open state (Fig. 5) based on several observations. First, top-ranked docking modes of PIPC1 (6.5 nM) were obtained against the open state, with an average docking score of –9.5 kcal/mol

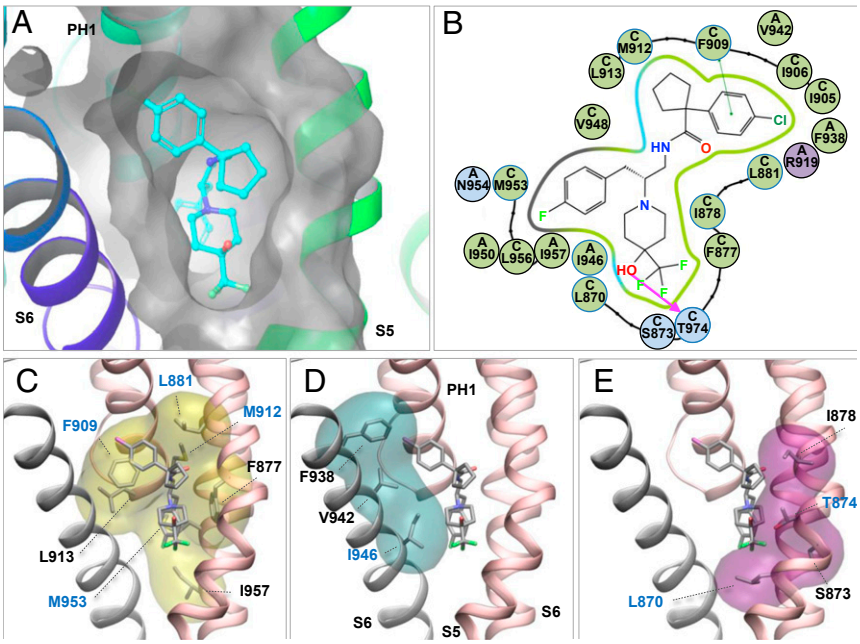

Fig. 5. Binding of PIPC to the open TRPA1 channel. (*A*) The PIPC binding site lies right below PH1, at the interface of 1 helical segment S5 with 2 helical segments S6, the latter from an adjacent subunit. The receptor surface is rendered in gray. Protein atoms are rendered as cartoons, colored by residue position (S6, blue; S5 and PH1, green). PIPC1 is shown in ball-and-stick rendering; carbon, oxygen, nitrogen, and halogen atoms are colored in cyan, red, blue, and green, respectively. (*B*) Two-dimensional map of PIPC1 interactions with TRPA1. Critical binding residues (blue circles) are confirmed by mutagenesis study (*SI Appendix*, Table S1). Green, light blue, and gray lines indicate hydrophobic, polar, and contact interactions; purple arrows indicate hydrogen-bonding interactions; dot-connecting dark green lines indicate π-stacking. Green and light blue petals indicate hydrophobic and polar residues. "A" and "C" in petals indicate adjacent TRPA1 subunits. (*C*–*E*) Critical binding residues are rendered as volumetric Gaussian density maps (at 0.5 density isovalue) in transparent mode. Maps in different colors indicate regions of the binding site that account for specific interactions with the bound ligand (licorice mode). Protein atoms are rendered in cartoon representation, with gray and pink indicating distinct and adjacent subunits. Critical binding residues are labeled in blue. For PIPC1, ligand protonation state was determined experimentally to be neutral; carbon, nitrogen, oxygen and hydroxyl group, chlorine, and fluorine atoms are colored in gray, blue, red, purple, and light green, respectively. Binding modes were validated by mutagenesis and SAR explorations (Schemes 1 and 2).

as opposed to the closed state, scoring only −6.9 kcal/mol (*SI Appendix*, Table S3). Both docking poses and scores were almost perfectly reproducible among each structure when comparing results obtained from different models (Fig. 5 *A* and *B* and *SI Appendix*, Fig. S4 *A* and *B* and Tables S2–S4). Remarkably, key molecular interactions, captured in these binding modes of PIPC1 to the open channel, were in line with observations derived from SAR studies (Scheme 1); additionally, in the top-ranked binding modes, ligand functionalities, critical for potency (e.g., the chlorobenzyl moiety and the substituted piperidine ring), were shown to interact with protein residues crucial for binding (i.e., F909 and I946), as determined experimentally (Fig. 5*B*). A similar trend was observed with PIPC2 (26 nM), which was found to have a docking score of −8.2 kcal/mol against the open channel, although no binding modes against the closed state were obtained in agreement with SAR data (*SI Appendix*, Fig. S4 *F* and *G* and Table S3). Regarding PIPC3 and PIPC4 (*SI Appendix*, Fig. S9 and Table S3), the 2 derivatives with lower potency, only poor docking score, or no binding modes were obtained (*SI Appendix*, Table S3; also see *Impact of Protonation and Chirality on PIPC Binding* for details). Second, distributions of docking modes of PIPC1 and PIPC2 against the open (but not the closed) state revealed the presence of ensembles of almost identical binding conformations (56 and 52% of the total poses; *SI Appendix*, Table S2) around the top-ranked poses for each molecule, corresponding to the lowest energy minimum or best docking score. Third, changes in the predicted binding affinities of PIPC1 upon mutation of critical binding residues showed better correlation with experimental values when the binding occurs to the open than the closed TRPA1 channel (*SI Appendix*, Tables S1 and S5 and Plot S1). Importantly, these analyses also revealed specific residues important for agonist binding (see *Role of Individual Residues in TRPA1 Activation* for details). Lastly, for PIPC1 and PIPC2, systematic mutations of these residues in the open state resulted in systematic worsening of the relative docking solutions (*SI Appendix*, Table S6). Altogether, our computational results, along with SAR (Scheme 1) and mutagenesis data (*SI Appendix*, Table S1), support the hypothesis that PIPC1 and PIPC2 primarily bind to the open channel. Nonetheless, despite this large body of evidence that supports the binding of PIPCs to the open state of TRPA1, we could not completely rule out the possibility that PIPCs can also bind to the closed state (*SI Appendix*, Figs. S7–S10), although energetically it is less favorable (*SI Appendix*, Table S3).

In the open conformation, hydrophobic residues of PH1 (F909, M912, and L913) and the S5 and S6 segments (L881, F877, M953, and I957) form a deep cleft accommodating the bulk of PIPC1 and PIPC2 (Fig. 5 *B* and *C* and *SI Appendix*, Fig. S4). Both compounds are further stabilized by side chains located on S6 (F938, V942, and I946, from adjacent subunits) and by S5 residues (L870, S873, T874, I878, and L881) (Fig. 5 *C* and *E* and *SI Appendix*, Fig. S4). Additional hydrophobic/polar residues face the binding site from top (I905, I906) and bottom (N954) locations, though none of these residues engage directly in PIPC binding.

At the core of the hydrophobic cleft, residues F909, M912, M953, and F877 project 2 arms that provide stabilization to the main scaffold of PIPC1 and PIPC2 (Fig. 5*C* and Scheme 1). While F909 engages in π–π stacking with the chlorobenzyl ring (right-hand side; RHS), M953 and, marginally, M912 (PH1) stabilize the fluorobenzyl group at the opposite end (left-hand side; LHS)

via the fluorine bond with sulfur atoms in the methionine side chains. The neighboring residue F877 is also involved in this network, although only partially. Halogens on the peripheral functionalities are important for maintaining potency, and in particular the fluorine atom at the LHS (PIPC1 vs. PIPC2; PIPC3 vs. PIPC4). The L881–M912 pair, interacting with the cyclopentyl-amide moiety, also offers important stabilization. Two factors contribute to the stabilization of the piperidine ring. First, I946 on the S6 segment and L870 on the adjacent S5 helix offer hydrophobic stabilization to the -CF_3 moiety on the substituted piperidine ring (Fig. 5 *D* and *E*). Second, T874 (or alternatively S873, as found in additional docking modes) interacts via hydrogen bonding with the hydroxypiperidine group (Fig. 5*E*).

Impact of Protonation and Chirality on PIPC Binding. Hypothetically, the nitrogen on the piperidine ring can adopt a neutral or protonated state. The p*Ka* values of PIPC1 to 4 were determined to range from 5.91 to 6.16 (*SI Appendix*, Table S4); therefore, at the experimental condition (pH 7.4), 95 to 97% of compounds are in the neutral form. Interestingly, our computational modeling suggested that PIPC binding to the open TRPA1 channel is favored when the compounds are neutral (Fig. 5 and *SI Appendix*, Fig. S4). Compared with charged ligands (*SI Appendix*, Figs. S5 *B* and *D* and S6 *B* and *D*), binding of neutral compounds to the closed state is energetically less favorable (*SI Appendix*, Figs. S5 *A* and *C* and S6 *A* and *C*), though could not be ruled out completely (*SI Appendix*, Figs. S7 and S8). On the contrary, docking scores consistently indicate the closed state as the worst ranking solution for all tested PIPCs (*SI Appendix*, Tables S1–S3), a result in agreement with SAR data (Schemes 1 and 2). Together, these data support the notion that PIPC1 and PIPC2 bind to the open channel to exert their agonistic effect. We expect additional ligands in the same chemical class to adopt a similar binding behavior.

The SAR data showed that (*R*)-enantiomers PIPC1 and PIPC2 are significantly more potent than their respective (*S*)-counterparts PIPC3 and PIPC4 (Scheme 1). We elucidated, via computational modeling, the structural details for PIPC stereoselective binding. Binding modes of (*S*)-PIPCs (*SI Appendix*, Fig. S9) populate 2 distributions: The prevailing one contains miscellaneous poses where the piperidine ring is almost invariantly flipped upside-down (*SI Appendix*, Fig. S9, *Insets*), pointing toward the pore and compromising the interaction with T874 (Fig. 5 *B* and *E* and *SI Appendix*, Fig. S4). Consistent with this notion, T874A/N mutations reduced the potency of PIPC1 by >1,000-fold (*SI Appendix*, Table S1). Small fractions of poses (maximum 21%) match, albeit partially, the binding mode adopted by (*R*)-PIPCs (*SI Appendix*, Figs. S5 and S6). Docking scores were systematically worse for (*S*)-PIPCs than for (*R*)-counterparts (*SI Appendix*, Table S3).

Role of Individual Residues in TRPA1 Activation. Through human–rat chimera study and computational analysis, we identified a number of residues important for human TRPA1 activation by PIPCs (Fig. 5*B* and *SI Appendix*, Fig. S4). Additional mutagenesis studies were performed to further test our initial binding mode hypotheses (*SI Appendix*, Table S1). Experimental results were then complemented by computational predictions of changes in the binding affinity of PIPC1 for TRPA1 mutants in both open and closed states (*SI Appendix*, Plot S1). Our results showed that the effects of all mutations were reproduced computationally in the open but not the closed state. A quantitative agreement between experiment and computation was obtained for the open state. These data support the notion that PIPC1 binds to the open state (see the paragraph in *SI Appendix*, Plot S1 for details).

Additionally, by combining computational modeling with experiments, we characterized the molecular determinants of PIPC binding and activation of TRPA1 and gleaned insights from the mechanisms of agonist versus antagonist binding (*SI Appendix*, Table S5). The roles of V875, F909, I946, and other critical residues, including M912, I950, M953, L881, and L870, are discussed below.

Residue V875 on the S5 segment. V875 was previously shown to underlie the species-specific response of TRPA1 channels to menthol (31) and cold (30). In the current study, V875 was identified to be critical for TRPA1 activation by PIPCs (Fig. 3). Molecular modeling suggested that, in both the closed and open states, V875 points away from the allosteric site, therefore excluding a direct role of V875 in PIPC binding (Fig. 5). Molecular dynamics simulation of the closed state showed that V875 maintains its starting configuration for the entire time evolution (>400 ns), supporting the idea that V875 is not directly involved in binding. To further elucidate the role of V875, we replaced the valine residue with alanine or methionine (V875A, V875M) or with the helix-breaking residue proline (V875P) in addition to glycine (V875G in Fig. 3). As expected, V875A and V875M showed minimal changes in PIPC1 potency (~2-fold change; *SI Appendix*, Table S1), whereas V875P and V875G resulted in >700-fold or complete loss of effect, respectively (*SI Appendix*, Table S1). These findings, along with previous reports (30, 31), suggested that V875 contributes to channel gating by retaining helical structure, rather than playing a direct role in ligand binding.

Residue I946 on the S6 segment. We previously showed that I946 mediated species-specific responses to thioaminals (29) and, in the current study, we identified I946 as critical for response to PIPCs (Fig. 3 and *SI Appendix*, Fig. S4). Analyses of TRPA1

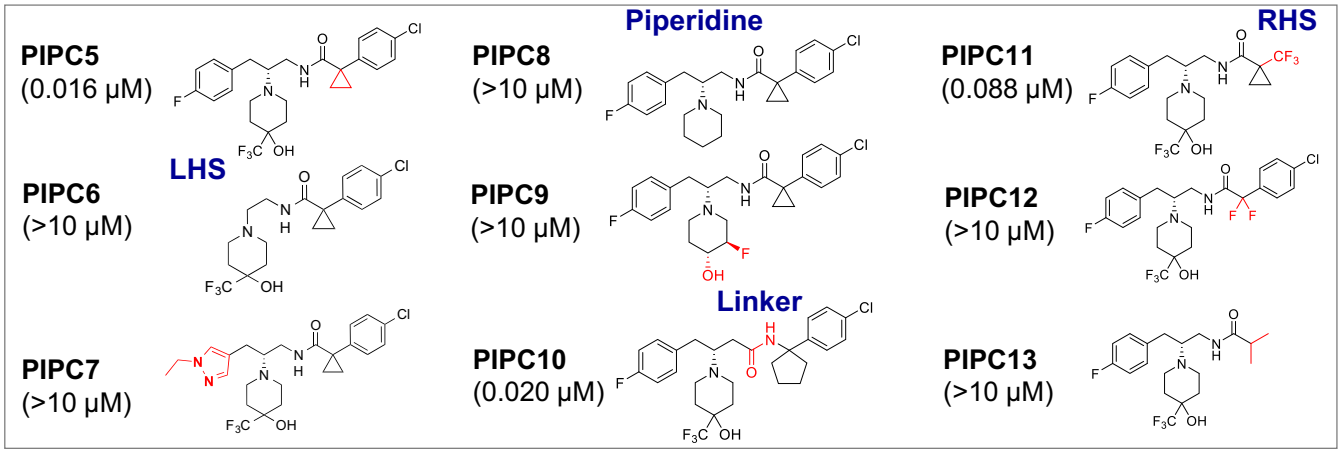

Scheme 2. Structure–activity relationship expansion for PIPC5 to PIPC13.

structures (open-state models using TRPV1 and TRPV6 as templates) indicated that residue I946 faces the binding site from an adjacent subunit (Fig. 5*B*, chain A versus chain C in petals and Fig. 5 *C*–*E*, gray cartoon and *SI Appendix*, Fig. S4*D*). Through computational docking, we also showed that I946 interacts directly with the substituted piperidine ring of all active (*R*)-PIPCs (Fig. 5 *B*–*E* and *SI Appendix*, Figs. S5 and S6). Conversely, no I946 involvement was predicted in the binding of inactive (*S*)-compounds (i.e., PIPC3 and PIPC4; *SI Appendix*, Fig. S9). Comparisons of open and closed TRPA1 states suggested that S6 shifts away from PH1 during channel opening (*SI Appendix*, Fig. S3). As a result, I946 faces a significantly wider allosteric site, capable of accommodating bulky chemical moieties (*SI Appendix*, Fig. S11). The I946M mutation reduced the size of the allosteric site, and consequentially resulted in a complete loss of effect on TRPA1 response to PIPC1 (*SI Appendix*, Tables S1 and S5 and Plot S1), a behavior that was confirmed computationally for the open (delta affinity 3.67 kcal/mol) but not the closed state (delta affinity 0.16 kcal/mol), a further indication that binding of PIPC1 occurs to the open TRPA1 channel.

Residue F909 on PH1. The F909A mutation was previously reported to abolish binding of A-967079 and general anesthetics (20, 32, 37). Computational modeling indicated that F909 projects its side chain right in the middle of the PIPC binding site. Analyses of PIPC1 and PIPC2 binding modes (Fig. 5 *B* and *C* and *SI Appendix*, Figs. S5, S6, S10, and S11*A*) suggested that F909 interacts, via π-stacking, with the peripheral chlorobenzyl substituent (RHS). Accordingly, the F909A mutation completely eliminated the activity of several PIPCs, consistent with computational docking results (*SI Appendix*, Tables S1 and S6).

Residue L881 on the S5 segment. Our modeling showed that L881 is located at the top of the binding site and interacts with the chlorobenzyl ring of PIPCs (Fig. 5 *B* and *C* and *SI Appendix*, Fig. S4). Mutating L881 to A resulted in nonfunctional channels. Interestingly, mutating L881 to I or V reduced the potency by several orders of magnitude (>1,200- and ∼150-fold, respectively), while mutations to smaller side chains (A or M) exerted only a mild effect on potency (*SI Appendix*, Tables S1 and S5 and Plot S1). Thus, we concluded that the presence of an additional methyl group on the Cβ-atom is deleterious for binding. Of note, the L881I mutation was previously shown to turn the antagonist A-967079 into an agonist (18).

Residue T874 on the S5 segment. Molecular docking indicated that T874, a V875-neighboring residue, is important for PIPC1 and PIPC2 binding. Specifically, T874 interacts via hydrogen bonding with the substituted piperidine ring to maintain potency (Fig. 5 *B* and *E* and *SI Appendix*, Fig. S4). Consistent with our binding mode hypothesis, the mutations T874A and T784N reduced PIPC1 potency by >1,700- and ∼2,300-fold, respectively (*SI Appendix*, Table S5 and Plot S1). Of note, a small, yet significant, fraction of PIPC1 docking poses suggested that S873, another V875-neighboring residue, can also contribute important binding interactions (Fig. 5*B*). Interestingly, both S873 and T874 were previously shown to be critical for binding A-967079 and general anesthetics (20, 32, 37).

Residue L870 on the S5 segment. Our structural modeling showed that L870 faces the allosteric site in a cleft that accommodates the substituted piperidine ring of PIPC1 and PIPC2 (Fig. 5*E* and *SI Appendix*, Fig. S4). Although both the L870T and L870S mutations resulted in complete loss of function or expression (*SI Appendix*, Tables S1 and S5), computational studies, including binding modes of PIPC1 and PIPC2, as well as delta affinity predictions suggested that L870 establishes important interactions (hydrogen-bonding and/or hydrophobic) with the hydroxyl-trifluoromethyl moieties of PIPC1 and PIPC2 (Fig. 5 *B* and *E* and *SI Appendix*, Fig. S4*E*), thereby highlighting the critical role of L870 in PIPC binding. To the best of our knowledge, residue L870 has not been identified to interact with other ligands.

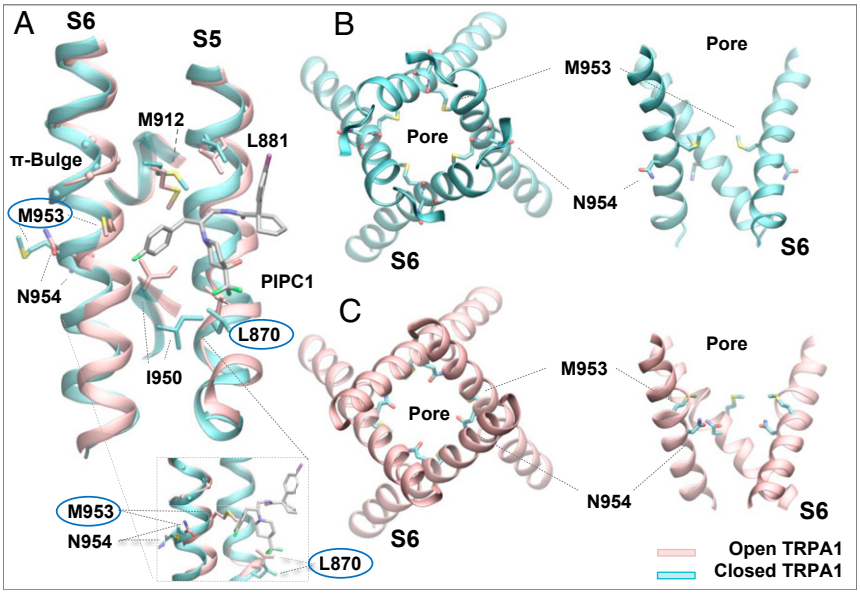

Fig. 6. Rearrangement of an evolutionarily conserved π-bulge on S6 results in differential sets of residues to face the pore and the PIPC binding site in TRPA1. (*A*) Superimposition of S5, S6, and PH1 helices in the closed and open TRPA1 states. Models were built on TRPV6 as templates. Critical residues undergoing structural rearrangements, namely M953 and N954, are highlighted in licorice mode. M953 faces the pore or the PIPC binding site in the closed or open states, respectively. N954 faces outside or inside the pore in the closed or open states, respectively. Additional residues responsible for differential binding of PIPC1 to the open and closed states are also shown, including L870, L881, M912, and I950. Residues that were not previously found to interact with other ligands (L870) or were only partially characterized (M953) are included in a blue circle. (*A*, *Inset*) Zoom into PIPC1 binding from a different angle and highlight of M953, N954, and L870. Protein atoms are rendered as in Fig. 4. (*B*) Top and lateral views of TRPA1 in the closed and open states, respectively. (*C*) S6 in 1 subunit was removed for visualization purposes.

Residue M912 on PH1. Computational docking suggested that M912 constitutes the back of the hydrophobic pocket by interacting with the spiro-cyclopentane moiety of PIPCs (Fig. 5 *B* and *C* and *SI Appendix*, Fig. S4). Consistently, the M912A mutation reduced PIPC1 potency by ∼25-fold. According to our binding affinity calculations, M912 is critically involved in the selective binding of ligands to the open state (*SI Appendix*, Table S5 and Plot S1), with a binding affinity change of 3.62 kcal/mol. In fact, our modeling suggests that, in the open TRPA1, M912 participates, along with M953, in the formation of critical fluorine bonds with halogenated phenyl rings (LHS) of PIPCs (Figs. 5 and 6 and *SI Appendix*, Fig. S4).

Residue I950 on the S6 segment. Located 1 helical turn from I946, I950 was predicted to be important for PIPC1 binding, offering important stabilization to the fluorobenzyl moiety (Fig. 5*B* and *SI Appendix*, Fig. S10). Accordingly, replacing I950 with a residue similar in size (I950V) did not affect potency; however, introducing a more drastic change (I950A) resulted in complete loss of function or expression (*SI Appendix*, Table S1). Delta affinity calculations also suggested that I950 is important for selective binding of PIPC1 to the open channel (*SI Appendix*, Table S5 and Plot S1). Interestingly, both residue I950 and its neighbor I946 are located in the S6 segment subjected to π-bulge rearrangements (Figs. 4*B* and 6*A*).

Residue M953 on the S6 segment. According to our docking studies, M953 lies at the bottom of a hydrophobic cleft and interacts with the fluorobenzyl ring of PIPC1, a critical moiety to maintain potency (Fig. 5 *B* and *C*). Consequently, M953V (a minor change) resulted in a moderate change in potency (15.3-fold), whereas the M953A mutation resulted in a complete loss of activity (*SI Appendix*, Tables S1 and S5 and Plot S1). In the open state, the fluorophenyl ring on PIPC1 (a phenyl in PIPC2) gains stabilization by forming a noncovalent interaction with the side chains of M953 (fully interacting) and with the neighboring PH1 residue M912 (partially interacting) through a fluorine bond with the sulfur atoms in the methionine residues (Figs. 5 and 6*A* and *SI Appendix*, Figs. S4 and S10). Furthermore, in the absence of the halogen in PIPC2, the interaction with the phenyl ring was weaker than in the case of PIPC1, which explains the lower potency of PIPC2 (26 nM, compared with 6.5 nM for PIPC1) and also the relative inefficiency of the double-reversible mutation (rM949I/G878V) in restoring PIPC2 activity (Fig. 3 *B*–*G*). Importantly, M953 is located on helix S6 just 1 turn below the π-bulge rearrangement conserved among TRP channels (33, 38) (Fig. 6). In the open state, M953 faces the S5–S6–PH1 site. In the closed state, M953 is shifted toward the pore, impairing interactions with bound ligands. With reference to PIPC1 and PIPC2, such a rearrangement of M953 abolished interaction with the fluorophenyl in PIPC1 or the phenyl moiety in PIPC2. In other TRP channels, like TRPV1, an asparagine residue (N676) was shown to rotate toward the pore or to point far away from it (38, 39) as a consequence of the rearrangement in the conserved π-bulge. When N676 faced the lumen in the TM pore (open, conductive state), the channel became fully hydrated. Conversely, when N676 rotated out of the lumen, the pore became dehydrated (closed, nonconductive state). In TRPA1, the equivalent asparagine residue is N954, just 1 residue distant from M953. Here we hypothesize a similar mechanism: By interacting with M953, PIPC1 (and PIPC2) stabilizes a conformation of the π-bulge that allows the conserved asparagine (N954) to face the TM pore, hence leading to a conductive state (Fig. 6).

Despite facing the allosteric site, additional residues, including I878 (S5), I905 (PH1), I906 (PH1), F938 (S6), and V942 (S6), were not predicted to engage in direct interactions with PIPCs (Fig. 5). Mutating these residues to alanine had only 10-fold or less effect on potency (*SI Appendix*, Table S1).

SAR Expansion and Molecular Modeling. To further explore the TRPA1–PIPC interactions, we designed, synthesized, and tested additional analogs (Scheme 2 and *SI Appendix*, Schemes S1–S5). Results from molecular modeling were corroborated with experimental SAR data.

Molecular docking suggested that the spiro-cyclopentane alpha to the amide on the RHS of PIPC1 and PIPC2 does not interact directly with TRPA1 (Fig. 5 *B* and *E* and *SI Appendix*, Fig. S4 *B* and *E*–*G*). Consistent with this notion, a spiro-cyclopropane is well-tolerated at this position (PIPC5, IC_{50} = 16 nM), with only mild loss in potency compared with the spiro-cyclopentane (PIPC1, IC_{50} = 6.5 nM). Starting from PIPC5, we modified the LHS of the piperidine-carboxamide core (PIPC6 and PIPC7). Molecular docking suggested that the lipophilic LHS aryl group engages with TRPA1 via hydrophobic interactions and, in the case of LHS fluorinated PIPCs, fluorine–sulfur interactions with the side chains of I950 and/or M953 (Fig. 5*B*), 2 residues critical for PIPC activation (*SI Appendix*, Table S1). Indeed, truncation of the LHS aryl (PIPC6) or replacement by a polar pyrazole ring (PIPC7) caused a very steep loss of potency (IC_{50} > 10 μM).

Our binding poses suggest that the trifluoromethyl moiety on the substituted piperidine ring engages in hydrophobic interactions with L870 and I946, and the hydroxyl group interacts with T874 via hydrogen bonding (Fig. 5 *B*, *E*, and *D*). From SAR data, a modification on the piperidine ring by removing trifluoromethyl and hydroxyl moieties resulted in a severe loss in potency (PIPC8, IC_{50} > 10 μM). Similarly, concomitantly removing the trifluoromethyl substituent and adding the *p*-fluorine atom also resulted in dramatic potency loss (PIPC9, IC_{50} > 10 μM). These results highlight the critical role played by I946, T874, and L870 in PIPC binding.

Molecular modeling suggested the lack of interaction between the amide linker and TRPA1. To test this idea, we designed a synthetic route (*SI Appendix*, Scheme S5) and generated PIPC10, a linker reversed-amide compound (Scheme 2). Consistent with the molecular modeling, PIPC10 retained potency on TRPA1 (IC_{50} = 20 nM).

We then further explored the aryl ring at the RHS, which was suggested to interact with F909 via π-stacking (Fig. 5*B*). Replacing the aryl ring with a trifluoromethyl group resulted in a moderate loss in potency (PIPC11, IC_{50} = 88 nM). The spiro-cyclic ring (either spiro-cyclopropane or spiro-cyclopentane) at this position was predicted to enable bioactive orientation of attached substituents. Indeed, replacing this moiety with a gem-difluoro (PIPC12) or an isopropyl (PIPC13) group resulted in a complete loss in potency (IC_{50} > 10 μM).

Overall, our SAR data were consistent with computational predictions, therefore lending support to the binding modes (Fig. 5).

Discussion

In the present work, we studied a series of piperidine-carboxamide analogs via functional characterization, phylogenic analysis, computational modeling, and SAR exploration. Although some of these compounds were previously categorized as antagonists (28), we concluded that their primary function is the activation of human TRPA1 based on several lines of evidence. First, PIPCs induce TRPA1-specific Ca^{2+} influx; in contrast, the TRPA1 antagonist A-967079 only shows a blocking effect (Fig. 1 *A*–*C*). Second, PIPCs evoke TRPA1-specific currents in whole-cell patch-clamp recordings (Fig. 1 *D* and *E*). Third, the agonist effect can be attributed to specific domains (i.e., S5L and S6; Fig. 2) and specific residues (i.e., V875 and I946; Fig. 3). Of note, PIPC1/2 are partial agonists compared with AITC, and at high concentrations they desensitize TRPA1, resulting in an apparent block of AITC response (Fig. 1). These effects are reminiscent of the effect of 5-iodoresiniferatoxin on the TRPV1 channel: 5-Iodoresiniferatoxin exhibited partial agonist effect on TRPV1, but when coapplied with capsaicin (a full agonist), 5-iodoresiniferatoxin blocked capsaicin

response and therefore was long considered an antagonist (40). Desensitization is a common feature of TRPV1, TRPA1, and other TRP channels, but the detailed mechanism of desensitization is not well-understood. For TRPV1, the heat-induced desensitization involves conformational rearrangement of the pore (41), and the capsaicin-induced desensitization may result from the membrane depletion of PIP_2 (42). It will be interesting to explore whether similar mechanisms exist for PIPC-mediated desensitization of TRPA1.

PIPC1 activates human TRPA1 at the picomolar-to-nanomolar range, but does not have an effect on rat, dog, guinea pig, or chicken channels (Figs. 1*A* and 2*A*). Through characterizing human–rat TRPA1 chimeras and point mutations, we identified 2 critical residues (V875 and I946): V875G and I946M abolished human TRPA1 response to PIPC1 and PIPC2, whereas the reversal mutations (rG878V/M949I) conferred response to the rat channel (Fig. 3). Therefore, V875 and I946 are both necessary and sufficient in determining the species-specific effects. Through computational investigations, we identified a hydrophobic, druggable site located at the interface of PH1 with the helical segment S5 and 2 S6 helical segments (Fig. 5), which comprises residue I946 and is located in the proximity of residue V875. It is worthy of noting that our computational work was based on 2 independent sets of structural models. First, given that the only experimental structure of TRPA1 available to date was solved in the closed state, 2 models were built of TRPA1 in the open state using TRPV1 and TRPV6 as templates. Then, the experimental structure of the closed TRPA1 was refined by modeling unresolved amino acid segments and optimizing side-chain orientations. Last, 1 additional model of the closed TRPA1 state was obtained using TRPV6 as template. Remarkably, both sets of models (open and closed) yielded the same results that were further validated by experimental mutagenesis and SAR expansions, a clear indication that our computational work relied on solid ground.

There are several inherent limitations to our study. First, PIPC1 and PIPC2 appear much more potent in the Ca^{2+} assay than in patch-clamp experiments (Fig. 1 *C* and *E*), and this discrepancy could result from the difference in methodology and the difficulty of using patch clamp for quantitative analysis under the current conditions. The Ca^{2+} assay was conducted in Hanks balanced salt solution (containing 1.26 mM Ca^{2+} and 1.0 mM Mg^{2+}) and was able to assess concentration response in a quantitative manner. Patch-clamp experiments were performed in a nominally divalent-free condition to minimize channel desensitization. Even in the absence of Ca^{2+}/Mg^{2+}, pronounced desensitization still occurred in response to PIPCs, thereby underestimating their effects at higher concentrations. Also due to desensitization, currents were measured from a single stimulation in a single cell, averaged, and normalized against the currents of 100 μM AITC obtained from a different group of cells (Fig. 1*E*). The difficulty in quantitative analysis was further aggravated by the partial agonistic effect of PIPCs. Despite these limitations, patch clamp provided a qualitative, independent verification of PIPCs' effect on wild-type and mutant channels. Second, our work suggests a preferential binding of PIPCs to the open state, but could not completely rule out the possibility of closed-state binding. PIPCs induce channel desensitization, and such a mechanism is not currently elucidated. Third, there are 4 identical binding sites for PIPCs, yet it is unknown how many bound ligands are required to open TRPA1. The Hill slopes obtained from Ca^{2+} assays (e.g., 1.5 for PIPC1 and PIPC2; Fig. 1*C*) may indicate binding of multiple ligands, but the exact interpretation could be cofounded by positive or negative cooperativity and by the nonlinearity of the Ca^{2+} assay. For example, AITC potentially modifies many cysteine residues (e.g., C621, C641, and C665, in each of the 4 subunits), yet the Hill slope for AITC dose response is 1.4 (Fig. 1*C*). Alternative future approaches, such as ligand binding assays or concatenated hetero-tetrameric channels with 1 or more subunits containing a mutation to prevent ligand binding, should be explored to directly assess the stoichiometry of ligand binding. Fourth, due to the lack of open-state experimental structure, we decided to utilize molecular docking, mutagenesis analysis, and SAR exploration. Nevertheless, this iterated approach proved to be useful in delineating the molecular underpinnings of PIPC binding. In this regard, it is extremely interesting to note that the binding site of PIPCs (agonists) overlaps with the binding spot for the antagonist A-967079 (20) (*SI Appendix*, Fig. S3), and with that of the agonists propofol and isoflurane (37). Additionally, propofol and isoflurane were shown to interact with several residues important for PIPC binding—namely T874, F909, and M912. In addition to these common residues shared by multiple ligands, we identified a set of residues that are uniquely involved in PIPC binding or modulation. For example, L870 interacts with the hydroxyl-trifluoromethyl moieties of PIPCs (Fig. 5 *B* and *E* and *SI Appendix*, Fig. S5), and M953 forms a noncovalent interaction with the fluorophenyl ring on PIPC1 (a phenyl in PIPC2) to stabilize the open conformation. To the best of our knowledge, L870 has not been identified previously as interacting with other ligands; M953 was proposed to play a role in general anesthetic binding in our previous study (32) but was not tested experimentally. Hence, it will be interesting to test whether residues such as L870 and M953 can be exploited for compound optimization or agonist–antagonist conversion.

Remarkably, our study suggests that members of the TRP channel family share a conserved allosteric binding site despite their relatively low sequence identity (e.g., 11.7% between human TRPA1 and TRPML1 channels). For TRPML1, the agonist ML-SA1 binds to a hydrophobic cavity surrounded by residues on PH1, S5, and S6 (23), a site strikingly similar to the binding site of PIPC1 on TRPA1 (*SI Appendix*, Fig. S11). Comparisons of the open and closed structures of TRPML1 revealed a shift in the relative position of PH1 and the selectivity filter upon agonist binding, likely resulting in opening both the lower gate and the selectivity filter (*SI Appendix*, Fig. S11*B*). Furthermore, a critical amino acid coordinating agonist binding (F505) is located in the middle of S6, and forms, along with other residues, a conserved π-helix (^{505}FIYMV^{509}) (23). An equivalent π-helix exists in TRPA1 (^{946}IFVPI^{950}) and is involved in crucial interactions with PIPCs (Fig. 6 and *SI Appendix*, Fig. S10). Conformational transitions involving the π-helix segment have been observed for the activation of several members of the TRP family (26, 33, 34). Mechanistically, introducing a π-helix segment into an α-helix causes a mismatch in the hydrogen-bond pattern (from $i \rightarrow i + 4$ to $i \rightarrow i + 5$) and an ∼100° rotation of the helical section. Consequently, a local α- to π-helix transition changes the registry of pore-lining side chains, thus opening or closing the activation gate. In light of this mechanism, the functional effects of allosteric modulators could be attributed to their ability to favor or prevent this local rotation of S6: Small molecules binding to the neighborhoods of the π-bulge establish favorable interactions with side chains exposed either in the closed (antagonists) or open state (agonists). Even though A-967079 and PIPCs share common binding residues, A-967079 only blocks the channel, whereas PIPCs exert both agonistic and desensitizing effects. It is currently not known how TRPA1 channels transit from the open to desensitized state upon PIPC binding. Allosteric conformational changes in the permeation pathway and binding sites are expected but remain to be explored experimentally. Our computational modeling and mutagenesis experiments showed that I946 is located right in the center of the binding site and involved in the π-bulge rearrangement (Figs. 5 *B* and *C* and 6*A*). Due to this structural change, a rearrangement of the bottom half of S6 occurs that alters the size and shape of the binding site, thereby recruiting different sets of residues to interact with ligands (Fig. 6 and

SI Appendix, Fig. S10). In TRPA1, major changes occur in the orientation of the amino acid pair M953–N954, with M953 pointing toward the binding site or the pore lumen upon the open-to-closed transition (Fig. 6 *B* and *D*). Accordingly, N954, a conserved asparagine residue, known in other TRPs to be responsible for pore hydration (38, 39) in conductive channels, faces the pore lumen only in the open TRPA1 state. It is noteworthy that M953 stabilizes the most potent PIPCs by interacting with the fluorophenyl group, a moiety critical for potency.

Although ion channels have been regarded as promising drug targets, significant challenges remain due to limitations in screening technologies, complex and poorly understood ligand–channel interactions, and, most often, the paucities of desirable chemical moieties (43). Particularly for TRPA1, very few tractable chemical scaffolds exist and the mechanisms for ligand–channel interactions are poorly understood. To date, the discovery of allosteric modulators has been mostly serendipitous. While the vast majority of PIPCs were synthesized using routes similar to a previous report (28), we devised a route (*SI Appendix*, Scheme S5) to enable the chemical synthesis of reversed-amide derivatives (e.g., PIPC10). It is noteworthy that this route expanded the coverage of chemical space available to current TRPA1 agonists, thus enabling the design and synthesis of future PIPC derivatives. More significantly, we have corroborated computational predictions with SAR data and experimental mutagenesis studies and have uncovered common and differential channel–ligand interactions for agonists and antagonists. Although additional work is needed, our results demonstrate that the combination of experimental study and atomistic modeling may represent a crucial frontier in drug discovery efforts targeting TRPA1 and other ion channels.

Materials and Methods

Calcium Influx Assays and Electrophysiological Recordings. TRPA1 channels were cloned in the pcDNA3.1 Hygro vector. Generation of human–rat TRPA1 chimeras and point mutations and transient transfections were performed as reported previously (30). All constructs were characterized by at least 2 independent transfections. The calcium influx assay and whole-cell patch-clamp recordings were performed as reported previously (30, 44) and described in *SI Appendix*.

Reagents and Chemical Synthesis. PIPC1 to 4 were synthesized according to previously reported procedures (28). PIPC5 to 13 were synthesized via similar methods as in *SI Appendix*, Schemes S1–S5. A-967079 was prepared as reported previously (4); other compounds were obtained from Sigma-Aldrich.

Computational Modeling. The following TRPA1 structure models were built: closed TRPA1 (refined) using the human TRPA1 cryo-EM structure (Protein Data Bank [PDB] ID code 3J9P) as template (45); open TRPA1 (model 1) using the fully open TRPV1 structure in complex with RTX and DkTx as template (46); and open and closed TRPA1 on TRPV6 (models 2 and 3) using open and closed structures of TRPV6 as the templates (PDB ID codes 6BO8 and 6BOA) (26). Details can be found in *SI Appendix, Material and Methods*.

Data Availability Statement. All data are available in the manuscript and *SI Appendix*.

ACKNOWLEDGMENTS. We thank Fabien J. Roussel, Jonathan C. Killen, and Robert J. Maxey for synthetic efforts, Michael Sanguinetti for suggestions, and Khaled Elokely for discussions. This work was supported by Genentech, Inc., the National Institute of General Medical Sciences of the NIH (R01GM093290 and S10OD020095), and National Science Foundation (ACI-1614804 and CNS-1625061). This research includes calculations carried out on Temple University's high-performance computing resources and thus was supported in part by the National Science Foundation through Grant 1625061 and by the US Army Research Laboratory under Contract W911NF-16-2-0189.

1. S. E. Jordt *et al.*, Mustard oils and cannabinoids excite sensory nerve fibres through the TRP channel ANKTM1. *Nature* **427**, 260–265 (2004).
2. G. M. Story *et al.*, ANKTM1, a TRP-like channel expressed in nociceptive neurons, is activated by cold temperatures. *Cell* **112**, 819–829 (2003).
3. D. M. Bautista *et al.*, TRPA1 mediates the inflammatory actions of environmental irritants and proalgesic agents. *Cell* **124**, 1269–1282 (2006).
4. J. Chen *et al.*, Selective blockade of TRPA1 channel attenuates pathological pain without altering noxious cold sensation or body temperature regulation. *Pain* **152**, 1165–1172 (2011).
5. K. Y. Kwan *et al.*, TRPA1 contributes to cold, mechanical, and chemical nociception but is not essential for hair-cell transduction. *Neuron* **50**, 277–289 (2006).
6. C. R. McNamara *et al.*, TRPA1 mediates formalin-induced pain. *Proc. Natl. Acad. Sci. U.S.A.* **104**, 13525–13530 (2007).
7. B. Kremeyer *et al.*, A gain-of-function mutation in TRPA1 causes familial episodic pain syndrome. *Neuron* **66**, 671–680 (2010).
8. S. R. Wilson *et al.*, The ion channel TRPA1 is required for chronic itch. *J. Neurosci.* **33**, 9283–9294 (2013).
9. B. Liu *et al.*, TRPA1 controls inflammation and pruritogen responses in allergic contact dermatitis. *FASEB J.* **27**, 3549–3563 (2013).
10. E. Andrè *et al.*, Cigarette smoke-induced neurogenic inflammation is mediated by alpha,beta-unsaturated aldehydes and the TRPA1 receptor in rodents. *J. Clin. Invest.* **118**, 2574–2582 (2008).
11. J. Chen, D. H. Hackos, TRPA1 as a drug target—Promise and challenges. *Naunyn Schmiedebergs Arch. Pharmacol.* **388**, 451–463 (2015).
12. M. Bandell *et al.*, Noxious cold ion channel TRPA1 is activated by pungent compounds and bradykinin. *Neuron* **41**, 849–857 (2004).
13. K. Hill, M. Schaefer, TRPA1 is differentially modulated by the amphipathic molecules trinitrophenol and chlorpromazine. *J. Biol. Chem.* **282**, 7145–7153 (2007).
14. X. F. Zhang, J. Chen, C. R. Faltynek, R. B. Moreland, T. R. Neelands, Transient receptor potential A1 mediates an osmotically activated ion channel. *Eur. J. Neurosci.* **27**, 605–611 (2008).
15. A. Hinman, H. H. Chuang, D. M. Bautista, D. Julius, TRP channel activation by reversible covalent modification. *Proc. Natl. Acad. Sci. U.S.A.* **103**, 19564–19568 (2006).
16. L. J. Macpherson *et al.*, Noxious compounds activate TRPA1 ion channels through covalent modification of cysteines. *Nature* **445**, 541–545 (2007).
17. M. Trevisani *et al.*, 4-Hydroxynonenal, an endogenous aldehyde, causes pain and neurogenic inflammation through activation of the irritant receptor TRPA1. *Proc. Natl. Acad. Sci. U.S.A.* **104**, 13519–13524 (2007).
18. N. Banzawa *et al.*, Molecular basis determining inhibition/activation of nociceptive receptor TRPA1 protein: A single amino acid dictates species-specific actions of the most potent mammalian TRPA1 antagonist. *J. Biol. Chem.* **289**, 31927–31939 (2014).
19. K. Nakatsuka *et al.*, Identification of molecular determinants for a potent mammalian TRPA1 antagonist by utilizing species differences. *J. Mol. Neurosci.* **51**, 754–762 (2013).
20. C. E. Paulsen, J. P. Armache, Y. Gao, Y. Cheng, D. Julius, Structure of the TRPA1 ion channel suggests regulatory mechanisms. *Nature* **525**, 552 (2015).
21. E. Cao, M. Liao, Y. Cheng, D. Julius, TRPV1 structures in distinct conformations reveal activation mechanisms. *Nature* **504**, 113–118 (2013).
22. M. Li *et al.*, Structural basis of dual Ca^{2+}/pH regulation of the endolysosomal TRPML1 channel. *Nat. Struct. Mol. Biol.* **24**, 205–213 (2017).
23. P. Schmiege, M. Fine, G. Blobel, X. Li, Human TRPML1 channel structures in open and closed conformations. *Nature* **550**, 366–370 (2017).
24. X. Zhou *et al.*, Cryo-EM structures of the human endolysosomal TRPML3 channel in three distinct states. *Nat. Struct. Mol. Biol.* **24**, 1146–1154 (2017).
25. T. E. T. Hughes *et al.*, Structural basis of TRPV5 channel inhibition by econazole revealed by cryo-EM. *Nat. Struct. Mol. Biol.* **25**, 53–60 (2018).
26. L. L. McGoldrick *et al.*, Opening of the human epithelial calcium channel TRPV6. *Nature* **553**, 233–237 (2018).
27. Y. Yin *et al.*, Structure of the cold- and menthol-sensing ion channel TRPM8. *Science* **359**, 237–241 (2018).
28. D. C. Pryde *et al.*, The discovery of a potent series of carboxamide TRPA1 antagonists. *MedChemComm* **7**, 2145–2158 (2016).
29. J. Chen *et al.*, Molecular determinants of species-specific activation or blockade of TRPA1 channels. *J. Neurosci.* **28**, 5063–5071 (2008).
30. J. Chen *et al.*, Species differences and molecular determinant of TRPA1 cold sensitivity. *Nat. Commun.* **4**, 2501 (2013).
31. B. Xiao *et al.*, Identification of transmembrane domain 5 as a critical molecular determinant of menthol sensitivity in mammalian TRPA1 channels. *J. Neurosci.* **28**, 9640–9651 (2008).
32. K. A. Woll *et al.*, Sites contributing to TRPA1 activation by the anesthetic propofol identified by photoaffinity labeling. *Biophys. J.* **113**, 2168–2172 (2017).
33. M. A. Kasimova *et al.*, A consistent picture of TRPV1 activation emerges from molecular simulations and experiments. bioRxiv:10.1101/310151 (24 August 2018).
34. E. Palovcak, L. Delemotte, M. L. Klein, V. Carnevale, Comparative sequence analysis suggests a conserved gating mechanism for TRP channels. *J. Gen. Physiol.* **146**, 37–50 (2015).
35. T. Halgren, New method for fast and accurate binding-site identification and analysis. *Chem. Biol. Drug Des.* **69**, 146–148 (2007).
36. T. A. Halgren, Identifying and characterizing binding sites and assessing druggability. *J. Chem. Inf. Model.* **49**, 377–389 (2009).

37. H. T. Ton, T. X. Phan, A. M. Abramyan, L. Shi, G. P. Ahern, Identification of a putative binding site critical for general anesthetic activation of TRPA1. *Proc. Natl. Acad. Sci. U.S.A.* **114**, 3762–3767 (2017).
38. M. A. Kasimova *et al*., Ion channel sensing: Are fluctuations the crux of the matter? *J. Phys. Chem. Lett.* **9**, 1260–1264 (2018).
39. M. A. Kasimova, D. Granata, V. Carnevale, Voltage-gated sodium channels: Evolutionary history and distinctive sequence features. *Curr. Top. Membr.* **78**, 261–286 (2016).
40. I. Shimizu, T. Iida, N. Horiuchi, M. J. Caterina, 5-Iodoresiniferatoxin evokes hypothermia in mice and is a partial transient receptor potential vanilloid 1 agonist in vitro. *J. Pharmacol. Exp. Ther.* **314**, 1378–1385 (2005).
41. L. Luo *et al*., Molecular basis for heat desensitization of TRPV1 ion channels. *Nat. Commun.* **10**, 2134 (2019).
42. B. Liu, C. Zhang, F. Qin, Functional recovery from desensitization of vanilloid receptor TRPV1 requires resynthesis of phosphatidylinositol 4,5-bisphosphate. *J. Neurosci.* **25**, 4835–4843 (2005).
43. E. Gianti, V. Carnevale, Computational approaches to studying voltage-gated ion channel modulation by general anesthetics. *Methods Enzymol.* **602**, 25–59 (2018).
44. W. Niforatos *et al*., Activation of TRPA1 channels by the fatty acid amide hydrolase inhibitor 3′-carbamoylbiphenyl-3-yl cyclohexylcarbamate (URB597). *Mol. Pharmacol.* **71**, 1209–1216 (2007).
45. C. E. Paulsen, J. P. Armache, Y. Gao, Y. Cheng, D. Julius, Structure of the TRPA1 ion channel suggests regulatory mechanisms. *Nature* **520**, 511–517 (2015).
46. Y. Gao, E. Cao, D. Julius, Y. Cheng, TRPV1 structures in nanodiscs reveal mechanisms of ligand and lipid action. *Nature* **534**, 347–351 (2016).